

Article

Diurnal Precipitation Features over Complex Terrains along the Yangtze River in China Based on Long-Term TRMM and GPM Radar Products

Suxing Zhu ^{1,2,*}, Chuntao Liu ² , Jie Cao ¹ and Thomas Lavigne ²

¹ Key Laboratory of Meteorological Disaster of Ministry of Education/ILCEC/Collaborative Innovation Center on Forecast and Evaluation of Meteorological Disasters, Nanjing University of Information Science and Technology, Nanjing 210044, China; 003542@nuist.edu.cn

² Department of Physical and Environmental Sciences, Texas A&M University-Corpus Christi, Corpus Christi, TX 78412, USA; chuntao.liu@tamucc.edu (C.L.); thomas.lavigne@tamucc.edu (T.L.)

* Correspondence: zhusuxing@nuist.edu.cn

Abstract: Based on the 20-year high-resolution precipitation data from TRMM and GPM radar products, diurnal features over complex terrains along the Yangtze River (YR) are investigated. Using the Fast Fourier Transform (FFT) method, the first (diurnal) and second (semi-diurnal) harmonic amplitude and phase of precipitation amount (PA), precipitation frequency (PF), and intensity (PI) are analyzed. The diurnal amplitudes of PA and PF have a decreasing trend from the west to the east with the decreasing altitude of large-scale terrain, while the semi-diurnal amplitudes of PA and PI depict the bimodal precipitation cycle over highlands. For the eastward propagation of PA, PF is capable of depicting the propagation from the upper to the middle reaches of YR, while PI shows the eastward propagation from the middle to the lower reaches of YR during nighttime and presents sensitivity to highlands and lowlands. According to the contribution of different-sized precipitation systems to PI over the highlands and lowlands, the small ($<200 \text{ km}^2$) ones contribute the least while the large ones ($>6000 \text{ km}^2$) contribute the most, but the medium ones ($200\text{--}6000 \text{ km}^2$) show a slightly larger contribution over the highlands than over the lowlands. The propagation of each scaled precipitation system along the YR is further analyzed. We found that small precipitation systems mainly happen in the afternoon without obvious propagation. Medium ones peak 2–4 h later than the small ones, with two eastward propagation directions at night from the middle reaches of YR to the east. The large ones are mainly located in lowlands at night, with two propagation routes in the morning over the middle and lower reaches of YR. Such a relay of the propagation of the medium and large precipitation systems explains the eastward movement of PI along the YR, which merits future dynamic studies.

Keywords: diurnal precipitation features; complex terrains; Yangtze River; TRMM & GPM product



Citation: Zhu, S.; Liu, C.; Cao, J.; Lavigne, T. Diurnal Precipitation Features over Complex Terrains along the Yangtze River in China Based on Long-Term TRMM and GPM Radar Products. *Remote Sens.* **2023**, *15*, 3451. <https://doi.org/10.3390/rs15133451>

Academic Editor: Ali Behrangji

Received: 31 May 2023

Revised: 4 July 2023

Accepted: 4 July 2023

Published: 7 July 2023



Copyright: © 2023 by the authors. Licensee MDPI, Basel, Switzerland. This article is an open access article distributed under the terms and conditions of the Creative Commons Attribution (CC BY) license (<https://creativecommons.org/licenses/by/4.0/>).

1. Introduction

Diurnal variation of precipitation is important to local weather and climate [1]. It is the major component of convective activity and also the primary criterion to test the performance of numerical models [2–6]. In general, over the ocean, precipitation is mainly from late evening to early morning; over land, precipitation dominates in the afternoon [7,8]. Meanwhile, regional differences around the world are distinct in the diurnal cycle of rainfall [9–12], especially under the influence of mountains [13–17].

China is a vast country with mountainous areas. Diurnal precipitation features over different regions of China have been widely investigated. Over North China, the spatiotemporal features of rainfall are highly correlated with elevation heights. Precipitation propagates from the mountains to the southeastern foothills and plains with two major peak times, one in the afternoon and the other in the early morning [18,19]. Over South China,

Southwestern China encounters nocturnal-morning rainfall, and Southeastern China is dominated by afternoon rainfall [20]. Rainfall corridors develop locally at night and extend to Central China during predawn, then induce convection at their northern terminus, which is the middle and lower reaches of the Yangtze River (YR) [17,21].

Over Central China, along the YR, its terrain gradually decreases from the west to the east with three-step terrain, which can be named as large-scale terrain. Many unique precipitation events are triggered by terrain, such as the well-known nocturnal rainfall in the Sichuan Basin [22,23], afternoon thermal convection in the Dabie Hill region [24], and morning Meiyu in the lower reach of YR [25] during the warm season. These precipitation events present an eastward propagation along the YR in rainfall diurnal phase [4,9,26], and these local topographies can be named as small-scale terrain (shown in Table 1). Many past studies have discussed the diurnal precipitation features with local small-scale terrain separately or with the large-scale terrain of the whole YR area. However, they have not paid adequate attention to the details of precipitation features with complex large- and small-scale topography along the YR. Meanwhile, in some cases, the long-duration rainfall can propagate from the upper to the lower reach of YR [15,27]. In other cases, nocturnal heavy rainfall in the upper reaches is not always followed by early morning heavy rainfall in the middle reaches of YR during summer [9]. And some researchers found that the diurnal peak originating from the eastern edge of the Tibetan Plateau is only able to propagate to the middle reach of YR during Meiyu periods [28]. With the numerical model, the early-morning rainfall in the lower reach of the YR arises from a local growth of rain events rather than migrating events from the middle reach [29]. However, it is still not clear how the propagation of precipitation over complex terrain along the YR works. These previous studies were mainly limited by the resolution of rain gauge records, reanalysis data, or case simulation analysis.

During the past two decades, remote sensing techniques have been rapidly developed in the area of quantitative precipitation [30,31]. The precipitation radars onboard the Tropical Rainfall Measurement Mission (TRMM) [32] satellite, which was launched in November 1997, carry the first space-borne Precipitation Radar (PR). With coverage of 36°S–36°N, the TRMM Ku band PR had a sensitivity of approximately 18 dBZ to detect precipitation [33]. After TRMM PR was turned off, observations of precipitation from space-borne precipitation radar were carried on by the new generation Global Precipitation Measurement (GPM) [34] core observatory satellite in February 2014. Instruments on board include the Dual-frequency Precipitation Radar (DPR), which operates at Ku (13.5 GHz) and Ka (35.5 GHz) bands with coverage to higher latitudes (65°S–65°N). The near-surface precipitation rates have been derived using the near surface radar reflectivity [33,35]. Therefore, since 1998, more than 20 years of Ku-band PR precipitation retrievals have been collected globally with high spatial resolution. They can provide a significant number of samples to investigate the changes in precipitation globally [36] and the detailed relationship between precipitation and topography diurnally [37]. In China, TRMM captures well the nocturnal peak over the eastern periphery of the Tibetan Plateau and the late-afternoon peak in southern China [38]. GPMs are assimilated to improve rainfall simulation associated with landfalling tropical cyclones [39], and they can exhibit microphysical features of precipitation [40]. Both TRMM and GPM show a high correlation coefficient with gauge observations over Central China [41].

In addition, the size of the precipitation systems is directly related to their life cycle, as short-/long-lived rainfall systems generally correspond to small-/large-scale rainfall [42]. The diurnal characteristics of different-sized precipitation systems in the 35°S–35°N land and ocean domain [10], over South America [12], and over Asia [3] have been discussed. Chen et al. [43] observed that small/large rainfall systems peak in the noon-to-early afternoon/evening hours. Analyzing precipitation systems of different scales over complex terrains will help us further understand the propagation of precipitation along the YR.

In this study, in Section 2, the topographical elevation data with study regions, TRMM and GPM Ku-band Radar Precipitation Features (KuRPFs) data, Ku-band 20-year 0.1° radar

precipitation data, and methodologies are presented. In Section 3, we first validate the Ku-band 20-year 0.1° radar precipitation data in the applications along the YR in China, then the diurnal variations of precipitation features, including precipitation amount, frequency, and intensity, over large- and small-scale terrains and the propagation of precipitation features over complex terrains along the YR are conducted. Using KuRPFs data, different scales of precipitation systems over complex terrains are analyzed to obtain the detailed terrain effect on precipitation intensity in Section 4. Conclusion and discussion are given in Sections 5 and 6, respectively.

2. Data and Methods

2.1. Global Topographical Elevation Data

The global topographical elevation data (GTOPO30_2MIN), with a horizontal grid resolution of 120 arcsec, are used to categorize the large-scale terrain as well as the details of the small-scale terrain along the YR in central-eastern China.

From west to east, the terrain along the YR (purple line in Figure 1) is complicated and unique. The river originates from the 1st step terrain (higher than 2000 m, upper reaches of YR) in China, which is headed by the Tibetan Plateau, and flows through the 2nd step (around 1000–2000 m, middle reaches of YR) and the 3rd step terrain (around 0–1000 m, lower reaches of YR) in China around 30°N . In the meantime, many small-scale terrains are located along the YR over the 2nd and 3rd step terrain, including six highlands and three lowlands in Table 1.

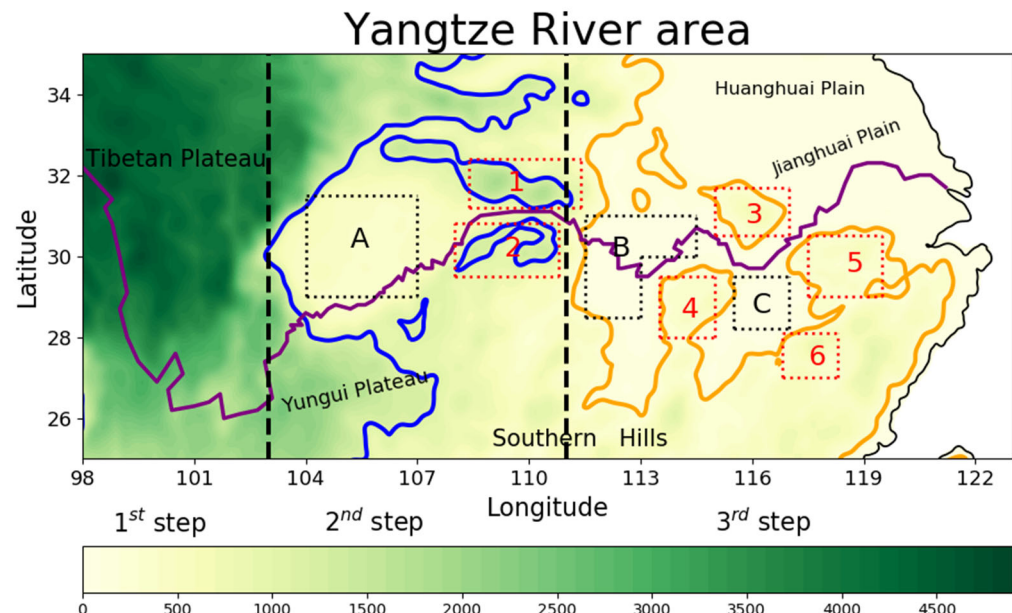


Figure 1. Geographical distribution of the topography in the Yangtze River area. The location of the Yangtze River is shown in purple. The black dash lines show the general border (103°E and 111°E) of the 2nd step terrain. The contours of 1100 (blue)/200 (orange) m are overlaid, representing small-scale terrain over the 2nd/3rd step terrain, i.e., three lowlands A–C (black dot line) and six highlands 1–6 (red dot line).

Table 1. Geographical names of lowlands and highlands in Figure 1.

Topographic Step	Lowlands	North Highlands	South Highlands
2nd step	A: Sichuan Basin	1: Daba Mountain	2: Wu Mountain ¹
3rd step	B: Lianghu Basin	3: Dabie Hill	4: Jiuling Hill ²
3rd step	C: Poyanghu Basin	5: Yellow Hill	6: Wuyi Hill

¹ Including Wu Mountain and Fangdou Mountain. ² Including Jiuling Hill and Mufu Hill.

2.2. TRMM and GPM KuRPFs and Their Algorithms

The 20-year TRMM and GPM Ku-band Radar Precipitation Features (KuRPFs) are defined by grouping the contiguous pixels with nonzero near-surface precipitation derived from the Ku-band radar carried either by TRMM or by the GPM satellite based on the algorithm proposed by Liu et al. [44]. The variables used in this study include local time, geographical center location, size (area of contiguous rain region), and volumetric rainfall for each KuRPF. Volumetric rain is calculated by multiplying each of the KuRPFs' average rain rate by its size in square kilometers, in units of $\text{km}^2\text{mm/h}$. In this study, features of different scaled precipitation systems are analyzed over the region of interest.

2.3. TRMM and GPM Ku-Band 0.1° Radar Precipitation Retrievals

In this study, 16-year satellite data from January 1998 to December 2013 of TRMM PR version 7 data and 4-year radar data from April 2014 to March 2018 of GPM Ku-band version 5 data are used. During the 16-year history of TRMM, there were some missing data in August 2001 due to a satellite orbital boost and in June 2009 due to a small technical issue. In order to produce a full 16-year data set, we have replaced these two months of data with August and June of 2014 TRMM data. We have chosen this method of replacing the missing data so that each month is represented equally in the sampling and no seasonal bias is introduced. Assuming the interannual variability is negligible due to the climatological nature of the study, the data from 2014 should be equivalent to the missing month. Then, 20 years of TRMM and GPM Ku-band radar near surface rain rate and their sample area, including the rain area and volume after taking into account sampling pixel sizes, are composited into local hourly precipitation properties for each month of the year, with a resolution of $0.1^\circ \times 0.1^\circ$. Though there are slight differences in the detection sensitivity before and after the boost of TRMM PR as well as the GPM KuPRF retrievals, this is not a big concern in the diurnal variation after the composite of 20 years of data [37]. And it is reasonable to study the spatial distribution of diurnal precipitation properties at 0.1° resolution [45].

2.4. Methodology for Diurnal Precipitation Features

With the above 20-year composite TRMM and GPM 0.1° hourly radar precipitation retrievals, the variables representing diurnal precipitation features are calculated at each 0.1° grid point during the warm season (April–August). These 20-year warm season hourly variables include the mean Precipitation Amount (PA—unconditional precipitation rate), the mean Precipitation Frequency (PF), and the mean Precipitation Intensity (PI—conditional precipitation rate). They are calculated as follows:

$$\text{PA} = \text{rain volume}/\text{sample area} \quad (1)$$

$$\text{PF} = \text{rain area}/\text{sample area} \quad (2)$$

$$\text{PI} = \text{rain volume}/\text{rain area} \quad (3)$$

Thus,

$$\text{PA} = \text{PF} \times \text{PI} \quad (4)$$

Here, the overall distribution of diurnal PA over the YR region and the diurnal variation of PA, PF, and PI over each small-scale terrain along the YR during the 20-year warm season are analyzed.

2.5. Methodology for Diurnal Amplitude and Phase

To quantify the diurnal characteristics of PA, PF, and PI, we conduct a Fourier harmonic analysis of the climatological diurnal PA, PF, and PI, which has been used in past studies [2,8,37]. Using the Fast Fourier Transform (FFT), we calculate the amplitude and

phase of hourly precipitation at each $0.1^\circ \times 0.1^\circ$ grid point for the above 3 precipitation features. The discrete FFT is calculated as follows:

$$F(u) = \frac{1}{24} \sum_{h=0}^{23} R(h) e^{-i\pi u h / 24} \quad (5)$$

where $F(u)$ is the Fourier component for the u th harmonic mode and $R(h)$ is the hourly PA/PF/PI value at the local hour, h . Thus, the amplitude of the u th harmonic mode A_u is given as:

$$A_u = 2 \times |F(u)| \quad (6)$$

A_u indicates the percentage deviation of the u th harmonic mode from the mean. In this study, the diurnal amplitude is the first harmonic mode A_1 in each grid point, and the second harmonic amplitude A_2 is also discussed.

The phase of the u th harmonic mode φ_u is given as follows:

$$\varphi_u = 24 \tan^{-1}(F(u)) \% 24 \quad (7)$$

where $\% 24$ indicates a modulo operation with respect to 24.

Figure 2 shows the flowchart of TRMM and GPM Ku-band 0.1° radar precipitation data, then using the data to analyze diurnal precipitation features (PA, PF, and PI) and their corresponding amplitude and phase.

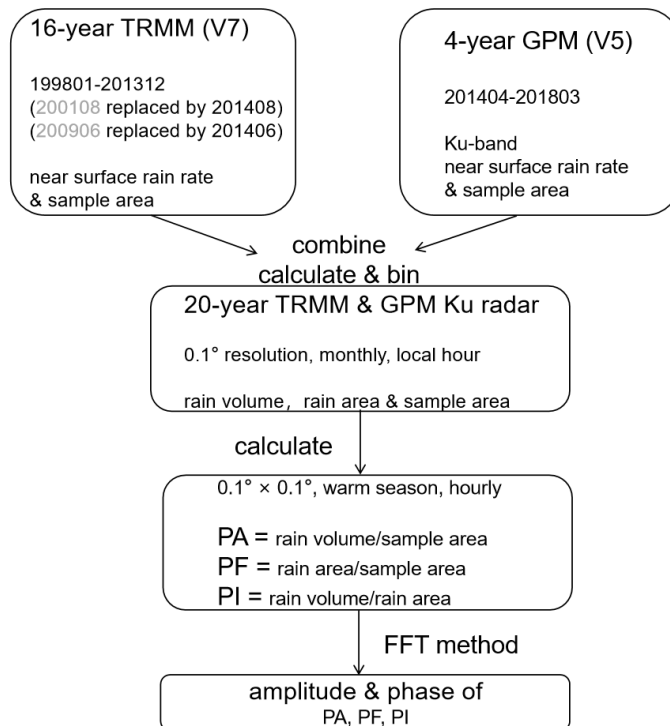


Figure 2. Flowchart of 20-year TRMM and GPM Ku-band radar precipitation retrievals (Section 2.3) and the following precipitation characteristic analysis method (Section 2.4 and 2.5).

3. Diurnal Precipitation Features along the YR

The overall distribution of PA using the hourly Ku-band radar precipitation data along the YR region is shown in Figure 3. Consistent with well-known climatic phenomena along the YR based on stationary and reanalysis data, diurnal precipitation features associated with the large-scale and small-scale terrains are evidently shown as follows: Firstly, from late evening to early morning (Figure 3a–c,h), there is heavy rainfall over the lowlands. To be specific, the well-known nocturnal rainfall over Sichuan Basin (Box A in Figure 1), Lianghu Basin (Box B), and Poyanghu Basin (Box C) is evident in Figure 3b during 03–

06 Local Time (LT). Jianghuai Plain mostly experiences heavy precipitation in the early morning (Figure 3c). A southwest-northeast oriented heavy rain belt is over the Southern Hills of the 2nd step terrain during 03–09 LT (Figure 3b,c). Secondly, heavy precipitation is concentrated over highlands, such as Daba Mountain (Box #1), Wu Mountain (Box #2), Dabie Hill (Box #3), Jiuling Hill (Box #4), and Wuyi Hill (Box #6), from noon to afternoon (Figure 3e,f). Meanwhile, the Southern Hills of the 3rd step terrain experience severe precipitation. Thirdly, weak rainfall occurs over the southeastern part of the Tibetan Plateau during 12–21 LT (Figure 3e–g). This proves the validity of the long-term remote sensing data in the applications over the YR in China.

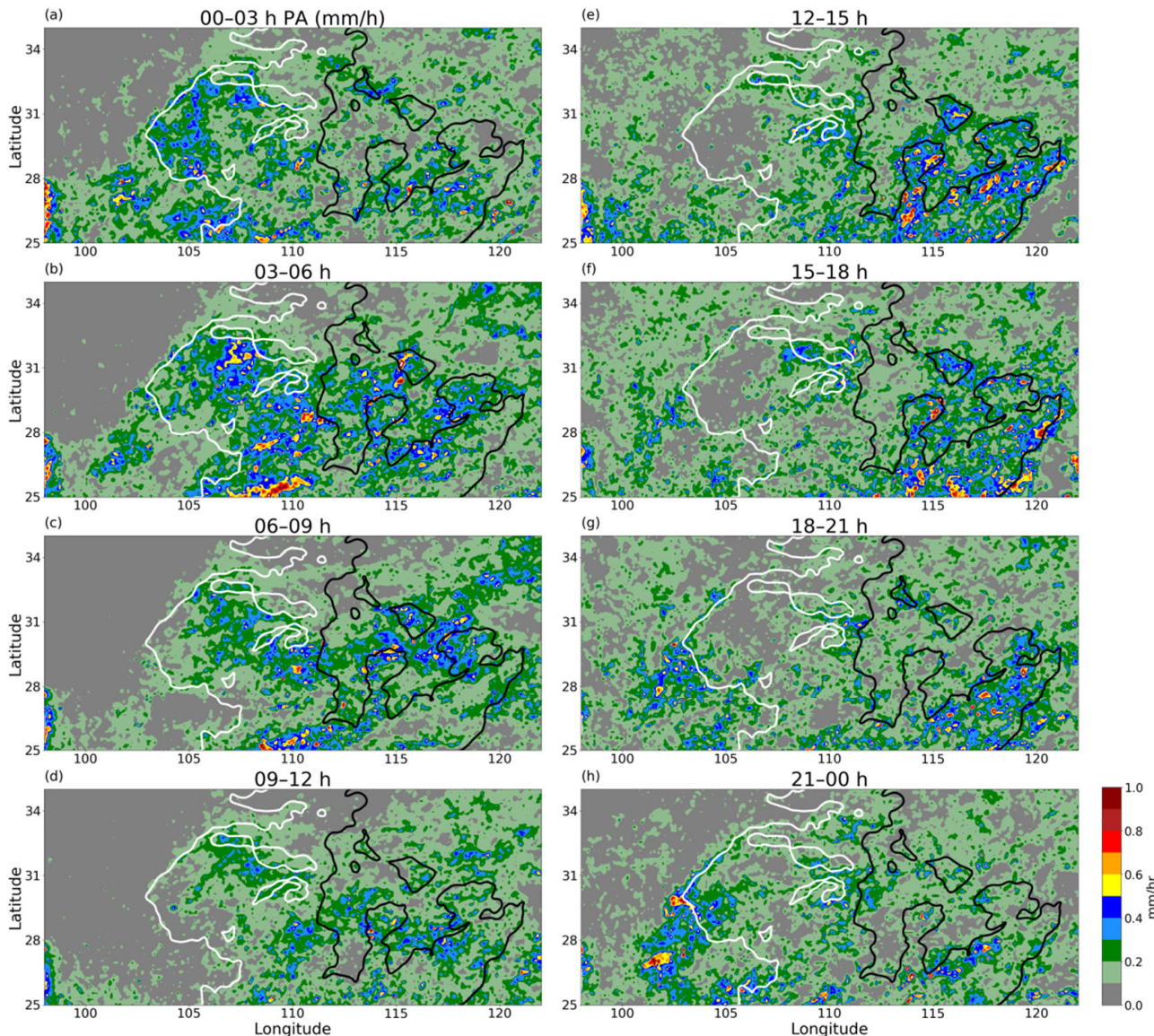


Figure 3. Distribution of every 3 h mean precipitation amount over the Yangtze River region during April–August with 20-year radar data. (a) 00–03 hr; (b) 03–06 hr; (c) 06–09 hr; (d) 09–12 hr; (e) 12–15 hr; (f) 15–18 hr; (g) 18–21 hr; and (h) 21–00 hr local time. The contours of 1100 m (white) and 200 m (black) terrain heights are overlaid.

3.1. Amplitude and Phase of PA, PF, and PI Diurnal Variation

The above diurnal features are based on the total distributions of PA, which is the combination of PF and PI. To further analyze their main intensities of diurnal and semi-diurnal amplitudes, Figure 4 shows their first and second harmonic amplitudes.

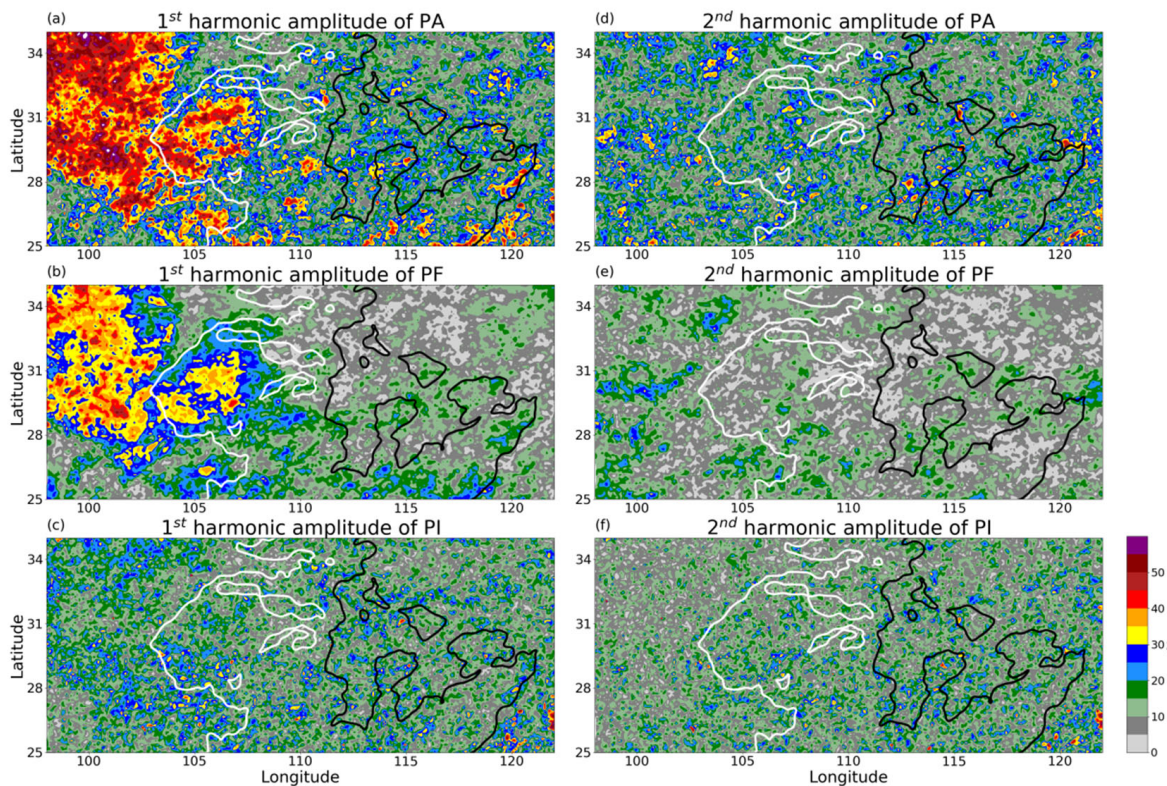


Figure 4. Distribution of diurnal amplitude of precipitation amount (a,d), precipitation frequency (b,e), and precipitation intensity (c,f), based on the ratio percentage of amplitude between FFT first (a–c)/second (d–f) fit and mean. The contours of 1100 m (white) and 200 m (black) terrain heights are overlaid.

The first amplitude of PA (Figure 4a) decreases gradually from the 1st to the 3rd step terrain, and this pattern agrees well with the diurnal amplitude of PF (Figure 4b). It is the largest over the Tibetan Plateau, with values greater than 30%. The Sichuan Basin and Yungui Plateau have values between 20% and 35%. The 3rd step terrain is the weakest, at approximately 0–15%. In contrast, PI (Figure 4c) is relatively uniform and weak over each step of terrain, with a value of 5–25% along the entire YR region. Therefore, the amplitude of PF dominates the main diurnal pattern.

The second harmonic amplitude of PA is well distributed in Figure 4d. The range is about 10–30% which is smaller than that of the first one. The amplitude of PF (Figure 4e) is even smaller. PI (Figure 4f) is larger than PF, with an increasing trend in amplitude from the 1st to the 3rd step terrain, especially over Dabei and Jiuling Hill. Therefore, the bimodal cycle of precipitation is obvious over the highlands in the 3rd step terrain, while PI mainly dominates this pattern.

Based on the distributions of diurnal precipitation features, the diurnal variation of standardized PA, PF, and PI over three lowlands and six highlands is investigated and shown in Figure 5. In general, the diurnal amplitude of PA is the largest, whereas that of PI is the smallest, with the exception of Lianghu Basin. The similarity between PF and PA corresponds with the result of the first harmonic rainfall amplitude, as shown in Figure 4a–c. Over three lowlands (Figure 5a–c), the precipitation reaches a peak in the morning. To be specific, Sichuan Basin peaks at 03 LT, Lianghu Basin peaks at 05 LT, and Poyanghu Basin peaks at 09 LT from western YR to its eastern valley. In other words, there is a shift in peak time from early morning to morning. Poyanghu Basin (Figure 5c) has a secondary peak of rainfall in the afternoon. Over the highlands (Figure 5d–i), different features exist, with all the regions showing a bimodal distribution pattern that is in accordance with the diurnal second harmonic amplitude of precipitation (Figure 4d–f). One peak occurs in the afternoon at around 13–16 LT, and the other one in the morning at around 00–09 LT.

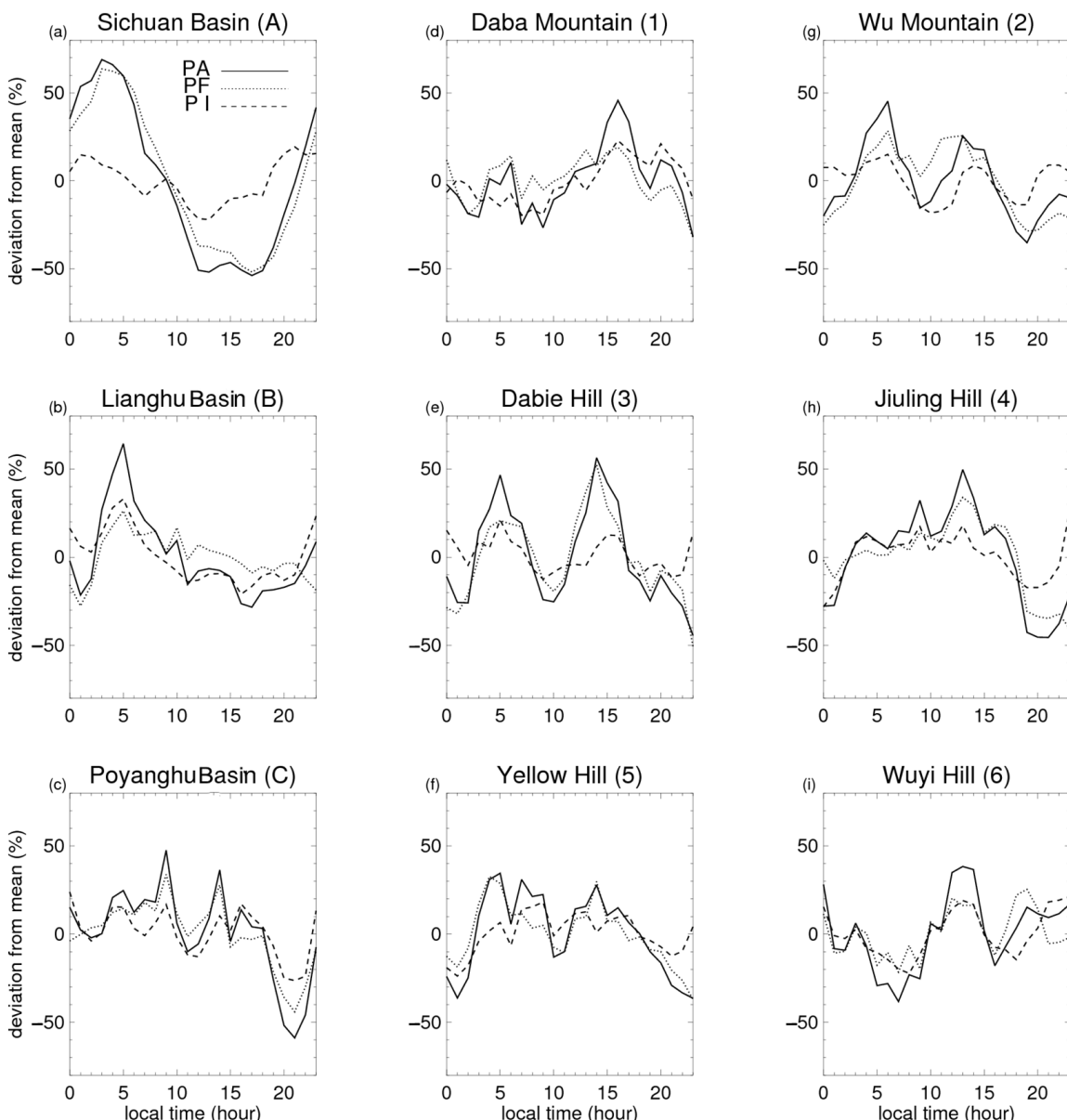


Figure 5. Diurnal variation of deviation from mean precipitation amount (PA), frequency (PF), and intensity (PI) over three lowlands (**a–c**) and six highlands (**d–i**) during the warm season. The lowland/highland areas correspond to the black/red dot line areas in Figure 1.

3.2. Propagation of PA, PF, and PI along the YR Region

To seize spatial-temporal variations of the shift in peak times over the three lowlands eastward along the YR, the Hovmöller diagrams of the three averaged precipitation properties over the area of 27° – 32.5° N are depicted as a function of longitude and local time.

As shown in Figure 6a, PA presents a weak afternoon rainfall over the Tibetan Plateau (west of 100° E) and exhibits a mid-night to early-morning propagation from the eastern Tibetan Plateau to the 2nd step terrain with an intensity of more than 0.3 mm/h. This propagation fades away from 108° E to the eastern Sichuan Basin. Near 108° – 111° E, which is the eastern edge of the 2nd step terrain, PA keeps the magnitude of 0.2 mm/h throughout the entire day while maintaining a relatively weaker intensity over western Lianghu Basin at 111° – 113° E, which is the western edge of the 3rd step terrain. The area east of 113° E, encompassing the lower reaches of the YR, exhibits two peaks in PA, which take place during 13–15 LT and 04–06 LT, respectively.

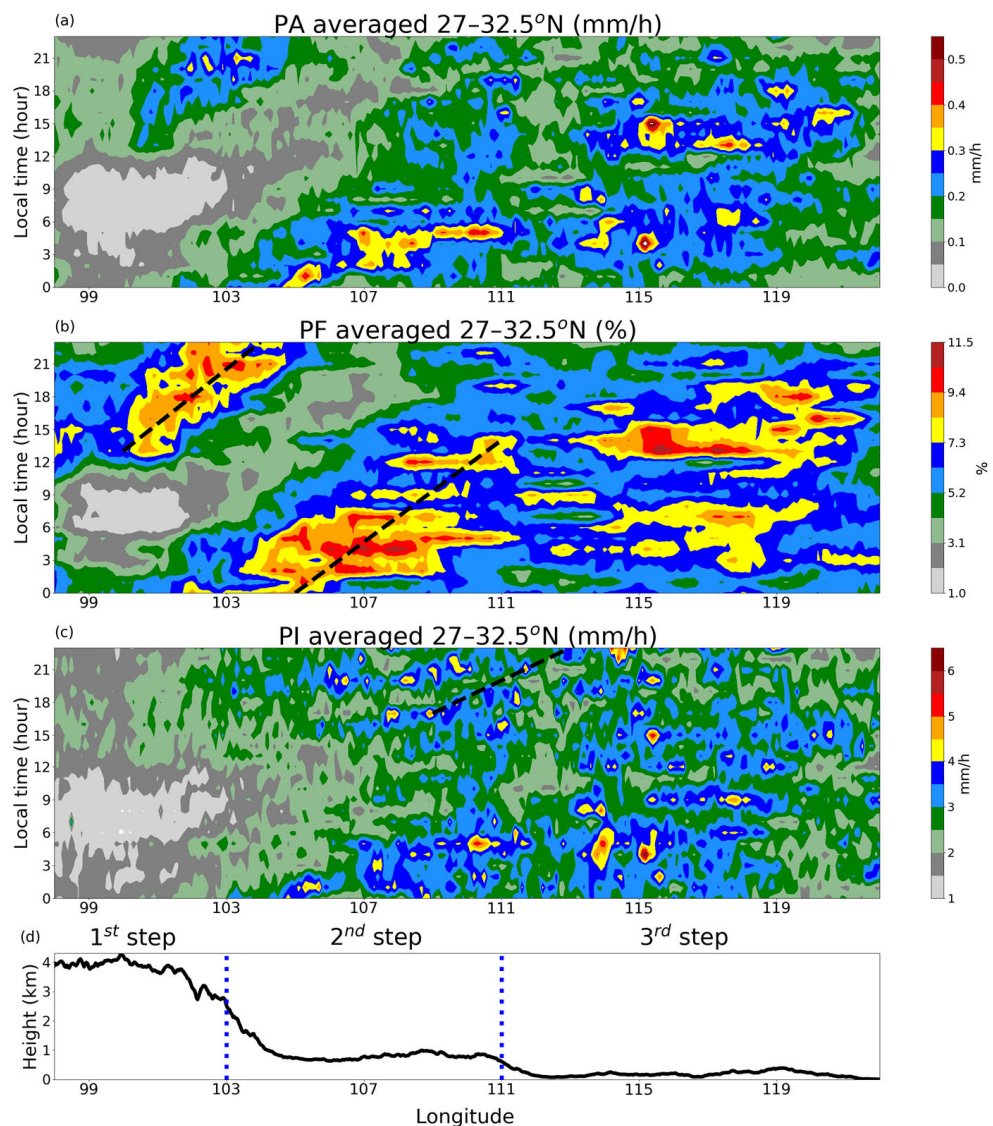


Figure 6. Diurnal average precipitation amount (a), frequency (b), and intensity (c) along the west-east cross section over the area of 27° – 32.5° N during the warm season. (d) is the mean topography of the same area with the boundary of three-step terrain (blue dot lines). The black dash lines highlight the propagation trails of precipitation.

The diurnal variation of PF (Figure 6b) exhibits a similar pattern to that observed in PA. The eastward propagation of nocturnal precipitation is more visible from the 1st to the 2nd steps of terrain. As denoted by dashed lines, PF centers travel from 100° E to 111° E from 13 LT until the next 14 LT. Over the lower reaches of YR east to 113° E, the afternoon rainfall (12–15 LT) occurs more frequently as a quasi-stationary mode.

The diurnal variation of PI (Figure 6c) displays a totally different pattern. The three strong PI centers at 110° E, 113.5° E, and 115.5° E at 05–06 LT, with a value greater than 5 mm/h, are over the 2nd and 3rd step terrain associated with three lowlands. They are consistent with the locations of three mesoscale precipitation centers identified by Chen et al. [21]. In addition, PI propagates through the junction of the 2nd and 3rd step terrain (109° – 113° E, dashed line) until the center of Lianghu Basin during 17–23 LT. Therefore, although PA and PF are weak over the western Lianghu Basin (111° – 113° E) throughout the day, PI is somewhat strong from late afternoon until midnight. And this heavy rainfall keeps the eastward propagation of precipitation from the 2nd to the 3rd step terrain, which closely follows the PF from the 1st to the 2nd step terrain.

4. Features of Diurnal Precipitation Systems of Different Sizes over Complex Terrains

4.1. Classification of the Scale of Precipitation Systems

Though sensitive to small-scale terrain (highlands and lowlands), as shown in the last subsection, PI is influenced by the intensity of precipitation systems at multiple scales over the targeted domain. Taking advantage of KuRPFs for separating precipitation systems by scales, Figure 7 provides the cumulative distribution function (CDF) and volumetric rain contribution of KuRPFs by size over lowlands and highlands to show the quantitative effects of small-scale terrain on PI. Both lowland and highland regions observe that approximately 80% of KuRPFs have a size less than 200 km^2 . Roughly 18% of KuRPFs have a size between 200 and 6000 km^2 ; only the top 1–2% have a size larger than 6000 km^2 . The scale distribution of precipitation systems follows power-law distributions, which correspond with Pope's [46]. For the volumetric rain contribution, the larger the horizontal scale of precipitation systems, the greater their contributions to the volumetric precipitation. Less than 200 km^2 have the smallest contribution to volumetric rain. The area between 200 and 6000 km^2 has a slightly larger contribution over the highlands when compared to the lowlands. The areas larger than 6000 km^2 have the largest contribution, and more over lowlands than over highlands. So the KuRPFs are classified into three categories: the small size (less than 200 km^2), the mid-size (between 200 and 6000 km^2), and the large size (greater than 6000 km^2). This scale classification is basically consistent with Hirose's [3,14].

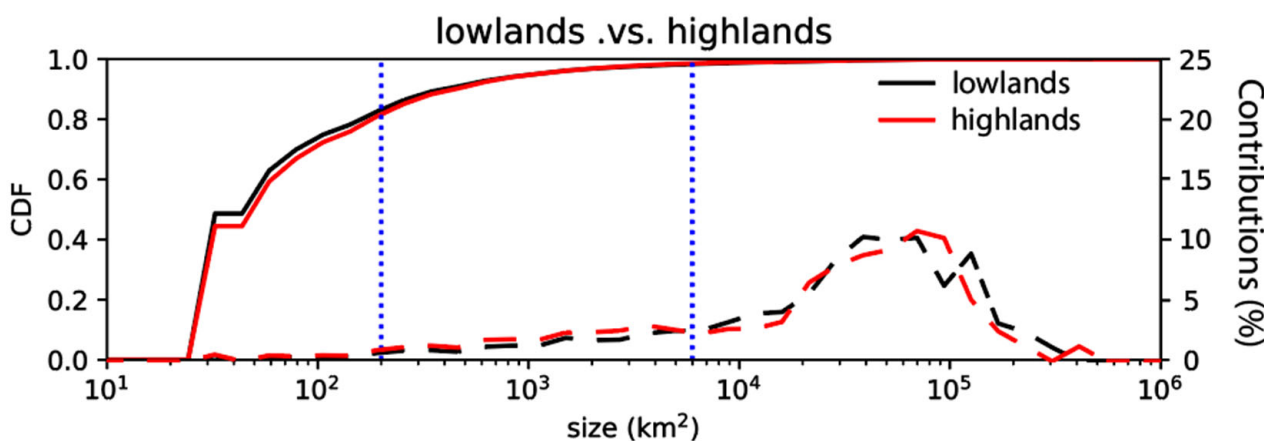


Figure 7. Cumulative distribution function (CDF, solid lines) and volumetric rain contribution (dashed lines) of KuRPFs by sizes over lowlands (black) and highlands (red) during the warm season. The 200 and 6000 km^2 shown in the blue dot lines denote the range for mid-size KuRPFs.

4.2. Contribution of Diurnal Precipitation Systems of Different Sizes over Small-Scale Terrain

To distinguish the different effects of small-scale terrain on small, medium, and large precipitation systems, the diurnal volumetric rain contribution from KuRPFs by size over lowlands and highlands is further calculated and shown in Figure 8. Small KuRPFs contribute the least across all regions throughout a day. Medium KuRPFs contribute a considerable amount to the afternoon precipitation (13–19 LT), especially over the highlands. And there is no significant difference in diurnal precipitation systems between the north and south highlands (Figure 8d,e). Large KuRPFs contribute the most to total precipitation over both lowlands and highlands throughout the entire day. Only over Sichuan Basin, there is a considerable gap in contribution from large KuRPFs during 13–21 LT, which may be evidence for Sichuan Basin being the source of eastward propagating precipitation. Therefore, precipitation systems of different sizes have distinctive contributions over lowlands and highlands.

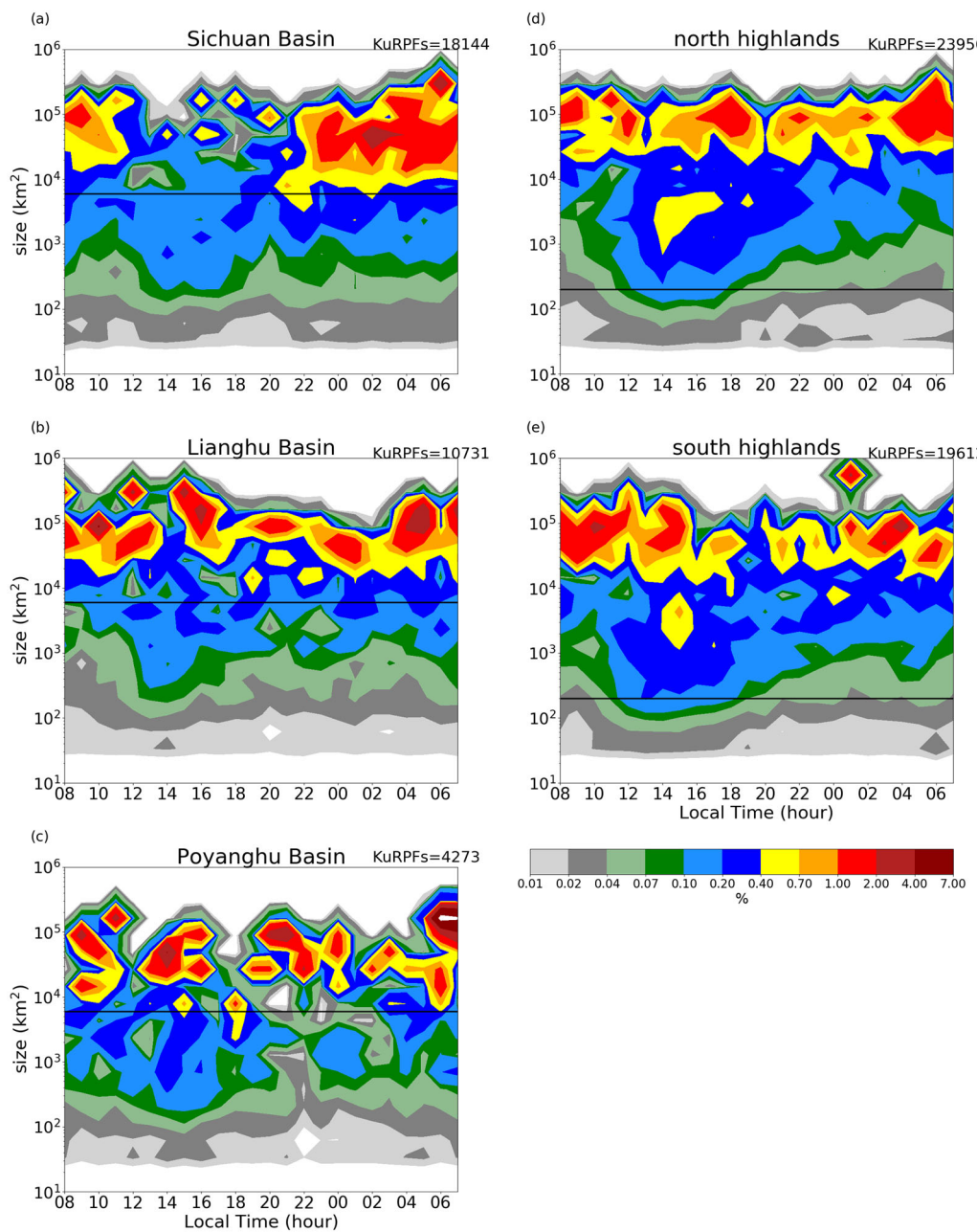


Figure 8. Diurnal volumetric rain contribution of KuRPFs by different sizes in Sichuan Basin (a), Lianghu Basin (b), Poyanghu Basin (c), north highlands (d), and south highlands (e) during the warm season. The black solid line in each panel shows the size of 6000/200 km² KuRPFs over lowlands/highlands. The value in the upper right corner of each panel represents the total number of KuRPFs, correspondingly.

4.3. Propagation of Different-Sized Precipitation Systems and Their Relationship with Complex Terrains

As shown in Figure 6c, PI presents eastward propagation from the 2nd to the 3rd step terrain (109° – 113° E) during 17–23 LT, and PI is the sum of all scaled precipitation systems' intensity. Here, we use volumetric rain to represent the intensity of each scaled precipitation system. Figure 9 calculates the diurnal average volumetric rainfall of each scaled KuRPF along the east-west cross section. Considering the difference in the horizontal scale of KuRPFs (Figure 7), the mean volumetric rainfall is gridded into different resolutions with the purpose of better representing different scales. To be specific, small KuRPFs are gridded into $0.25^{\circ} \times 0.25^{\circ}$ resolution, mid-size features into $0.5^{\circ} \times 0.5^{\circ}$, and large ones into $2^{\circ} \times 2^{\circ}$.

It is reasonable, as the monthly and hourly rain samples for each 0.2 grid point over an 8 yr period can have multiple precipitation systems [47].

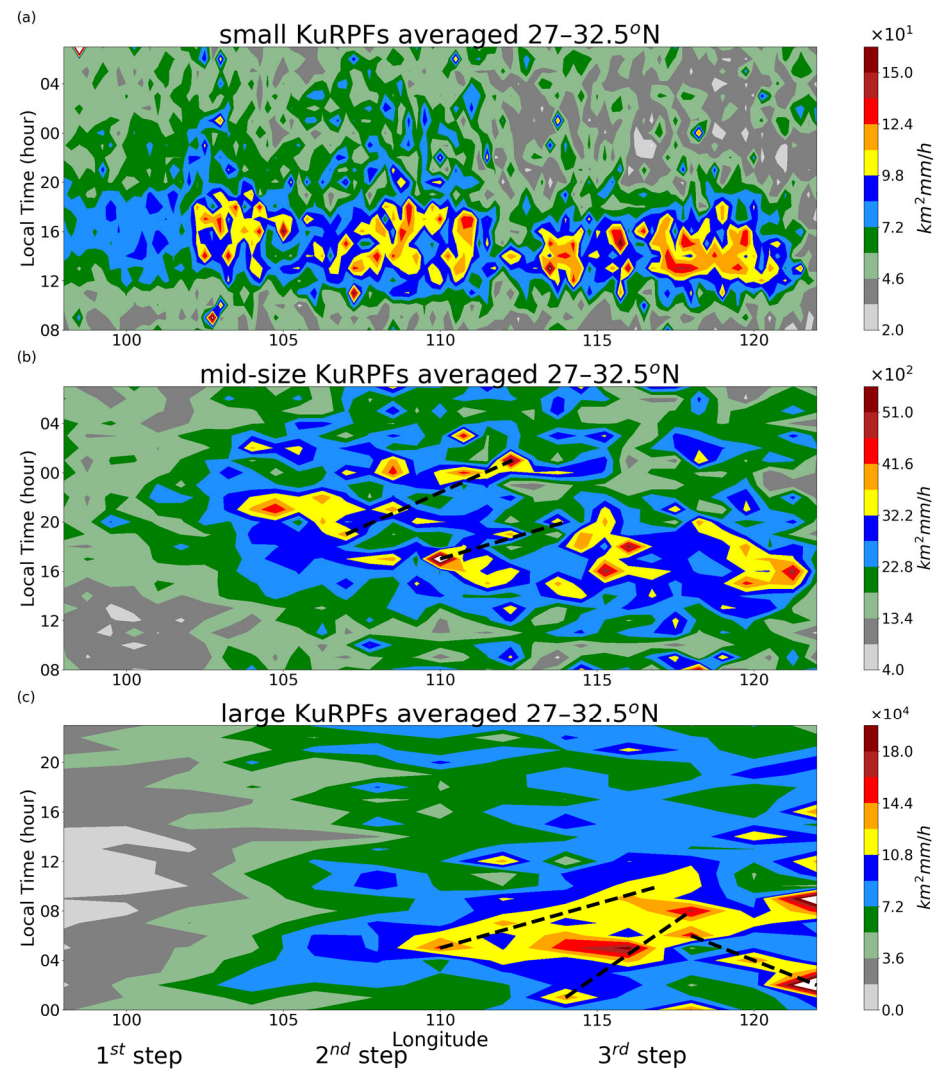


Figure 9. Diurnal average volumetric rain of small (a), mid-size (b), and large (c) KuRPFs along the west-east cross section over the area of 27° – 32.5° N during the warm season. The black dashed lines in (b,c) highlight the propagation trails of KuRPFs. Pay attention to the starting time in (c) is 00 LT.

In general, the position of each scaled KuRPF with its heavy volumetric rain moves eastward with the increase in their size. To be specific, small KuRPFs (Figure 9a) present moderate rain volumes of $72 \text{ km}^2 \text{mm/h}$ during 11–20 LT over all regions along the YR, especially in the afternoon. During that time, over the 2nd and 3rd steps of terrain, they even exhibit stronger rain volumes of $98 \text{ km}^2 \text{mm/h}$ without propagation characteristics. Medium KuRPFs (Figure 9b) show heavy rain volumes of $3220 \text{ km}^2 \text{mm/h}$ over the 2nd step terrain during 16–02 LT and over the 3rd step terrain during 13–22 LT. These medium KuRPFs may be born from small KuRPFs, as they peak 2–4 h later than small ones. Furthermore, the dash lines show that they can propagate eastward starting in the afternoon from the 2nd step terrain to the evening over the 3rd step terrain. In other words, one propagates from 107°E to 112°E during 19–01 LT, and the other from 110°E to 114°E during 17–20 LT. Large KuRPFs (Figure 9c) mainly have peak values in the early morning with heavy volumetric rain of $108,000 \text{ km}^2 \text{mm/h}$. The three centers occurring at 110°E , 116°E , and 118°E around 05–06 LT correspond to the three major propagation routes (dashed lines in Figure 9c) from mid-night to morning. Two of the three are eastward propagations. One

is from 110°E to 117°E during 05–10 LT, which is the movement from the eastern part of the 2nd step to the 3rd step terrain, and the other is from 114°E to 118°E during 01–08 LT, which is the eastward movement over the 3rd step terrain. The third major route is a westward propagating one from 122°E to 118°E during 02–06 LT, which is an inland propagation mode [20]. The propagation speed for the three routes is around 15–35 m/s, which is faster than previous total rainfall of 10–25 m/s [43,48]. Because large KuRPFs travel faster.

In order to explore the detailed propagation features of medium and large KuRPFs, Figure 10 gives the mean volumetric rain for medium and large precipitation systems during the prime time they occurred, respectively. As medium KuRPFs propagate mainly from late afternoon to midnight, it can be seen that strong rain volumes of $3900 \text{ km}^2 \text{ mm/h}$ occur over the Southern Hills of the 2nd step terrain and southeastern Sichuan Basin during 18–00 LT with gradually enhanced intensity (Figure 10a,b). Then at mid-night (00–03 LT), the maxima centers of medium KuRPFs move eastward to the boundary of the 2nd and the 3rd step terrain (Figure 10c). At the same time, large KuRPFs with rain volumes of $117,000 \text{ km}^2 \text{ mm/h}$ primarily happen around Dabie Hill over the 3rd step terrain (Figure 10d). Later, at 03–09 LT, the heavy precipitation centers continue propagating from Lianghu Basin to the eastern plain (Figure 10e,f). They are consistent with the two aforementioned eastward propagation routes (Figure 9c), and large KuRPFs continue the eastward propagation of medium ones in time and space, especially during 00–06 LT. Therefore, the relay propagation of medium and large KuRPFs over the 2nd and 3rd step terrain at mid-night can continue the eastward propagation of PI. It is also worth noting that in the 20-year warm season that we counted, every three hours the number of medium and large KuRPFs was about 10^4 and 10^3 , respectively (the same ratio as in Figure 7), which means the occurrence of large precipitation systems is very rare. This is why Xu et al. demonstrated that the diurnal cycle of precipitation features apparently propagates eastward from the eastern Tibetan Plateau for about 1000 km and does not continue to the eastern plain [49].

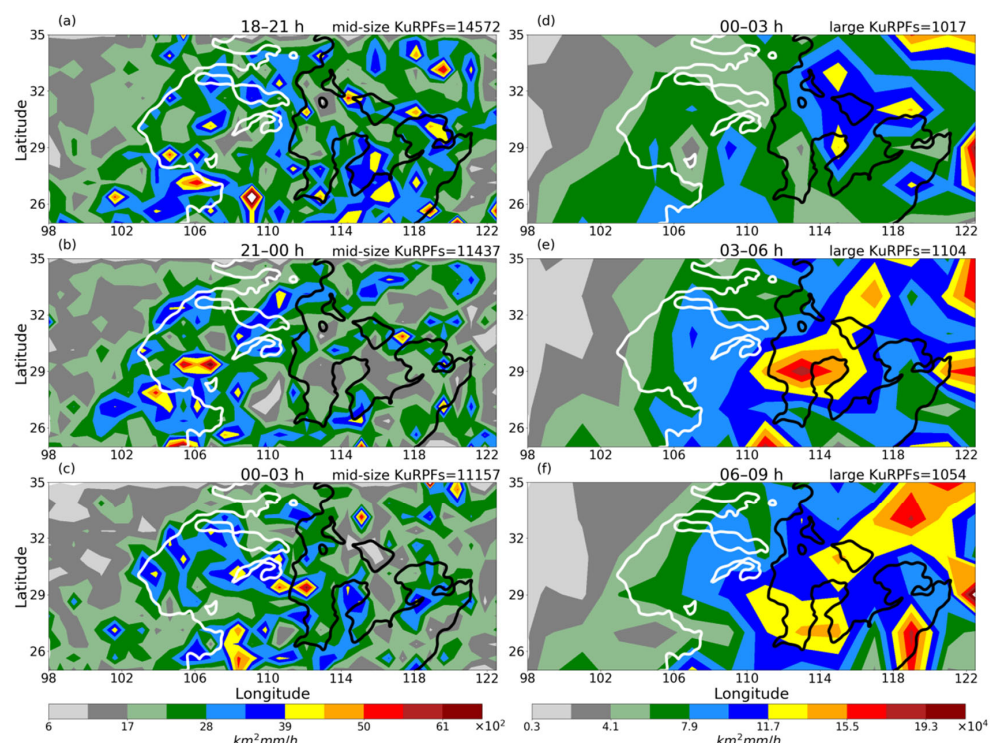


Figure 10. Distribution of 3 h mean volumetric rain per mid-size (a–c), and large (d–f) KuRPF during the warm season. (a) 18–21 hr; (b) 21–00 hr; (c,d) 00–03 hr; (e) 03–06 hr; and (f) 06–09 hr local time. The contours of 1100 m (white) and 200 m (black) terrain heights are overlaid. The value in the upper right corner of each panel represents the total number of KuRPFs, correspondingly.

5. Conclusions

The 16-year TRMM PR data combined with the 4-year GPM Ku-band PR data have been utilized to yield warm-season hourly precipitation data with a resolution of $0.1^\circ \times 0.1^\circ$. Six highlands and three lowlands (denoted as small-scale terrains) over the large-scale three-step terrain (corresponding to the upper, middle, and lower reaches of the Yangtze River) are selected as target regions to reveal the detailed diurnal precipitation features. Then the diurnal variations of precipitation amount (PA), precipitation frequency (PF), and precipitation intensity (PI) over complex terrains and their propagation along the Yangtze River (YR) with the influence of complex terrains are examined from the perspective of both the overall distribution of precipitation features and the separate characteristics of different-sized precipitation systems. The main findings are listed as follows:

Firstly, using the Fast Fourier Transform (FFT) method, the first and second harmonic amplitudes and phases of PF and PI are analyzed, focusing on their relative importance in revealing diurnal precipitation features. The first amplitude of PF shows the smoothly decreasing trend from the 1st step terrain all the way to the 3rd one, which dominates the main characteristics of PA associated with large-scale terrain. The second amplitude of PI depicts the bimodal precipitation cycle over the highlands, which reappears in the bimodal cycle in the second amplitude of PA. Therefore, PF and PI in PA both play important roles in depicting diurnal precipitation features associated with complex terrains.

Secondly, the Hovmöller diagrams of PF and PI are analyzed to seize their different capabilities in revealing the eastward propagation feature of PA. PF is only capable of depicting the precipitation propagation from the first step-terrain to the second one, while PI is from the second to the third during nighttime and presents sensitivity to highlands and lowlands.

Thirdly, with the adoption of TRMM and GPM Ku-band Radar Precipitation Features (KuRPFs) products, detailed terrain effects on PI in the view of different-sized precipitation systems are conducted. Precipitation systems are classified into three categories, i.e., small ($<200 \text{ km}^2$), medium ($200\text{--}6000 \text{ km}^2$) and large ($>6000 \text{ km}^2$), according to their contribution over lowlands and highlands. It is found that small and large precipitation systems contribute the least and the most over both lowlands and highlands, respectively. While medium ones have a larger contribution over highlands than over lowlands, especially in the afternoon. For the eastward propagation features along the complex YR, small ones are mainly initiated and developed locally over the 2nd and 3rd step terrains in the afternoon, without obvious propagation. The medium ones peak 2–4 h later than the small ones. Their two eastward propagation directions, which are the western one at midnight and the eastern one in the evening, contribute together to the propagation from the second-step terrain to the east. The peak values for large ones are shown over three lowlands from midnight to early morning. Two of the three march to the eastern plain in the morning from the second-step terrain to the third one or over the third-step terrain, which relays the propagation of medium ones from the second-step terrain at night. Thus, the relay propagation of medium and large precipitation systems over the 2nd and 3rd steps of terrain explains the eastward propagation of PI along the YR.

6. Discussion

The existing physical mechanisms of diurnal precipitation over complex terrains along the YR are mostly connected with the underlying surface. Including the thermally driven Mountain-Plain Solenoid (MPS) circulation due to different heating over the large-scale three-step terrain [28], Land Sea Breeze (LSB) with the inhomogeneous underlying surface [20], Mountain Valley Breeze (MVB) over small-scale terrain [18,24], and the Local Thermal Convection (LTC) with afternoon rainfall [4]. Moreover, the boundary layer Low Level Jet (LLJ) inertial oscillations provide moisture and the indirect updraft over Sichuan Basin and the lower reaches of the Yangtze River [21,23,25].

In addition, considering the background of large scale circulation, precipitation can propagate with the steering-level wind [42,48]. The southwest wind from the northwest

side of the west Pacific subtropical high [49] and the southwest wind ahead of the mid-level low trough east of the Tibetan Plateau [26] favor the eastward movement of rainfall during the warm season. With the help of westerly wind, from a PV perspective, it is found that mesoscale convective vortices may partially decouple up and down [50] or coalesce and re-separate over the middle and lower reaches of YR [51], and this causes heavy rainfall in the region.

In this study, solid observational evidence for the diurnal precipitation features along the YR of complex terrains is dug out. On the one hand, the conclusions are consistent with the above physical mechanism; on the other hand, the observation data can help us speculate about the possible eastward propagation of precipitation along the YR all the way to the eastern coast. From afternoon to the next afternoon, the propagation of precipitation from the upper to the middle reaches of YR is mainly reflected in the frequency, and the transition from the middle to the lower reaches is mainly manifested by the intensity of medium and large precipitation systems from afternoon to mid-night. These relay propagations of medium and large precipitation systems are key to continuing the eastward movement of precipitation, but their occurrence is very low compared with small ones. The following are large precipitation systems propagating over the lower reaches of YR until the ocean from early morning to morning. Dynamic studies on the dominant physical mechanism for the specific eastward propagating rainfall event will have other applications in the future.

Author Contributions: Conceptualization, S.Z., C.L. and J.C.; methodology, S.Z. and C.L.; software, S.Z. and C.L.; validation, S.Z.; formal analysis, S.Z.; investigation, S.Z.; resources, C.L. and S.Z.; data curation, C.L.; writing—original draft preparation, S.Z. and T.L.; writing—review and editing, S.Z. and J.C.; visualization, S.Z.; supervision, S.Z.; project administration, S.Z.; funding acquisition, S.Z. All authors have read and agreed to the published version of the manuscript.

Funding: The first author is grateful of financial support from the China Scholarship Council for visiting the Texas A&M-Corpus Christi. This work was also supported by NSFC-41105032.

Data Availability Statement: The high-resolution TRMM and GPM precipitation data and precipitation feature databases are available at: <http://atmos.tamucc.edu/trmm/data/> (accessed on 3 July 2023). The global topographical elevation data: <https://www.ngdc.noaa.gov/products/etopo-global-relief-mode> (accessed on 3 July 2023).

Acknowledgments: The authors want to thank the anonymous reviewers and editors for their comments on this paper.

Conflicts of Interest: The authors declare no conflict of interest.

References

1. Dai, A. Global precipitation and thunderstorm frequencies. Part II: Diurnal variations. *J. Clim.* **2001**, *14*, 1112–1128. [[CrossRef](#)]
2. Nesbitt, S.W.; Zipser, E.J. The diurnal cycle of rainfall and convective intensity according to three years of TRMM measurements. *J. Clim.* **2003**, *16*, 1456–1475. [[CrossRef](#)]
3. Hirose, M.; Nakamura, K. Spatial and diurnal variation of precipitation systems over Asia observed by the TRMM Precipitation Radar. *J. Geophys. Res.* **2005**, *110*, D05106. [[CrossRef](#)]
4. Yuan, W.; Yu, R.; Zhang, M.; Lin, W.; Chen, H.; Li, J. Regimes of diurnal variation of summer rainfall over subtropical east Asia. *J. Clim.* **2012**, *25*, 3307–3320. [[CrossRef](#)]
5. Chen, G.; Du, Y.; Wen, Z. Seasonal, interannual, and interdecadal variations of the East Asian summer monsoon: A diurnal-cycle perspective. *J. Clim.* **2021**, *34*, 4403–4421. [[CrossRef](#)]
6. Che Wan Zanial, W.N.; Malek, M.A.; Md Reba, M.N.; Zaini, N.; Ahmed, A.N.; Sherif, M.; Elshafie, A. Rainfall-runoff modelling based on global climate model and tropical rainfall measuring mission (GCM-TRMM): A case study in Hulu Terengganu catchment, Malaysia. *Heliyon* **2023**, *9*, e15740. [[CrossRef](#)] [[PubMed](#)]
7. Yang, S.; Smith, E.A. Mechanisms for diurnal variability of global tropical rainfall observed from TRMM. *J. Clim.* **2006**, *19*, 5190–5226. [[CrossRef](#)]
8. Liu, C.; Zipser, E.J. Diurnal cycle of precipitation, cloud, and lightning in the tropics from 9 years of TRMM observations. *Geophys. Res. Lett.* **2008**, *35*, L04819. [[CrossRef](#)]
9. Yu, R.; Zhou, T.; Xiong, A.; Zhu, Y.; Li, J. Diurnal variations of summer precipitation over contiguous China. *Geophys. Res. Lett.* **2007**, *34*, L01704. [[CrossRef](#)]

10. Liu, C. Rainfall contributions from precipitation systems with different sizes, convective intensities and durations over the tropical and subtropical. *J. Hydrometeor.* **2011**, *12*, 394–412. [[CrossRef](#)]
11. Biasutti, M.; Yuter, S.E.; Burleyson, C.D.; Sobel, A.H. Very high resolution rainfall patterns measured by TRMM precipitation radar: Seasonal and diurnal cycles. *Clim. Dyn.* **2012**, *39*, 239–258. [[CrossRef](#)]
12. Romatschke, U.; Houze, R.A., Jr. Characteristics of precipitation convective systems accounting for the summer rainfall of tropical and subtropical south America. *J. Hydrometeor.* **2013**, *14*, 25–46. [[CrossRef](#)]
13. Houze, R.A., Jr. Orographic effects on precipitating clouds. *Rev. Geophys.* **2012**, *50*, RG1001. [[CrossRef](#)]
14. Hirose, M.; Takayabu, Y.N.; Hamada, A.; Shige, S.; Yamamoto, M.K. Spatial contrast of geographically induced rainfall observed by TRMM PR. *J. Clim.* **2017**, *30*, 4165–4184. [[CrossRef](#)]
15. Wu, Y.; Huang, A.; Huang, D.; Chen, F.; Yang, B.; Zhou, Y.; Fang, D.; Zhang, L.; Wen, L. Diurnal variations of summer precipitation over the region east to Tibetan Plateau. *Clim. Dyn.* **2018**, *51*, 4287–4307. [[CrossRef](#)]
16. Sharifi, E.; Eitzinger, J.; Dorigo, W. Performance of the state-of-the-art gridded precipitation products over mountainous terrain: A regional study over Austria. *Remote Sens.* **2019**, *11*, 2018. [[CrossRef](#)]
17. Wu, R.; Chen, G.; Luo, Z.J. Strong coupling in diurnal variations of clouds, radiation, winds, and precipitation during the East Asian summer monsoon. *J. Clim.* **2023**, *36*, 1347–1368. [[CrossRef](#)]
18. Chen, M.; Wang, Y.; Gao, F.; Xiao, X. Diurnal variations in convective storm activity over contiguous North China during the warm season based on radar mosaic climatology. *J. Geophys. Res.* **2012**, *117*, D20115. [[CrossRef](#)]
19. Song, Y.; Wei, J. Diurnal cycle of summer precipitation over the North China plain and associated land-atmosphere interactions: Evaluation of ERA5 and MERRA-2. *Int. J. Climatol.* **2021**, *41*, 6031–6046. [[CrossRef](#)]
20. Jiang, Z.; Zhang, D.; Xia, R.; Qian, T. Diurnal variations of presummer rainfall over southern China. *J. Clim.* **2017**, *30*, 755–773. [[CrossRef](#)]
21. Chen, G.; Sha, W.; Iwasaki, T.; Wen, Z. Diurnal cycle of a heavy rainfall corridor over east Asia. *Mon. Wea. Rev.* **2017**, *145*, 3365–3389. [[CrossRef](#)]
22. Jin, X.; Wu, T.; Li, L. The quasi-stationary feature of nocturnal precipitation in the Sichuan Basin and the role of the Tibetan Plateau. *Clim. Dyn.* **2013**, *41*, 977–994. [[CrossRef](#)]
23. Zhang, Y.; Xue, M.; Zhu, K.; Zhou, B. What is the main cause of diurnal variation and nocturnal peak of summer precipitation in Sichuan basin, China? The key role of boundary layer low-level jet inertial oscillations. *J. Geophys. Res.* **2019**, *124*, 2643–2664. [[CrossRef](#)]
24. Wang, Q.; Xue, M.; Tan, Z. Convective Initiation by Topographically Induced Convergence Forcing over the Dabie Mountains on 24 June 2010. *Adv. Atmos. Sci.* **2016**, *33*, 1120–1136. [[CrossRef](#)]
25. Xue, M.; Luo, X.; Zhu, K.; Sun, Z.; Fei, J. The controlling role of boundary layer inertial oscillations in Meiyu frontal precipitation and its diurnal cycles over China. *J. Geophys. Res.* **2018**, *123*, 5090–5115. [[CrossRef](#)]
26. Yang, R.; Zhang, Y.; Sun, J.; Li, J. The comparison of statistical features and synoptic circulations between the eastward-propagating and quasi-stationary MCSs during the warm season around the second-step terrain along the middle reaches of the Yangtze River. *Sci. China Earth Sci.* **2020**, *63*, 1209–1222. [[CrossRef](#)]
27. Chen, H.; Yu, R.; Li, J.; Yuan, W.; Zhou, T. Why nocturnal long-duration rainfall presents an eastward-delayed diurnal phase of rainfall down the Yangtze river valley. *J. Clim.* **2010**, *23*, 905–917. [[CrossRef](#)]
28. Bao, X.; Zhang, F.; Sun, J. Diurnal variation of warm-season precipitation east of the Tibetan plateau over China. *Mon. Wea. Rev.* **2011**, *139*, 2790–2810. [[CrossRef](#)]
29. Cai, Y.; Lu, X.; Chen, G.; Yang, S. Diurnal cycles of Mei-yu rainfall simulated over eastern China: Sensitivity to cumulus convective parameterization. *Atmos. Res.* **2018**, *213*, 236–251. [[CrossRef](#)]
30. Levizzani, V.; Cattani, E. Satellite Remote Sensing of Precipitation and the Terrestrial Water Cycle in a Changing Climate. *Remote Sens.* **2019**, *11*, 2301. [[CrossRef](#)]
31. Costache, R.; Bao Pham, Q.; Corodescu-Roșca, E.; Cimpianu, C.; Hong, H.; Thi Thuy Linh, N.; Ming Fai, C.; Najah Ahmed, A.; Vojtek, M.; Muhammed Pandhiani, S.; et al. Using GIS, Remote Sensing, and Machine Learning to Highlight the Correlation between the Land-Use/Land-Cover Changes and Flash-Flood Potential. *Remote Sens.* **2020**, *12*, 1422. [[CrossRef](#)]
32. Kummerow, C.; Barnes, W.; Kozu, T.; Shiue, J.; Simpson, J. The Tropical Rainfall Measuring Mission (TRMM) sensor package. *J. Atmos. Oceanic Technol.* **1998**, *15*, 809–817. [[CrossRef](#)]
33. Iguchi, T.; Kozu, T.; Kwiatkowski, J.; Meneghini, R.; Awaka, J.; Okamoto, K. Uncertainties in the rain profiling algorithm for the TRMM precipitation radar. *J. Meteor. Soc. Jpn.* **2009**, *87A*, 1–30. [[CrossRef](#)]
34. Hou, A.Y.; Kakar, R.K.; Neeck, S.; Azbarzin, A.A.; Kummerow, C.D.; Kojima, M.; Oki, R.; Nakamura, K.; Iguchi, T. The Global Precipitation Measurement mission. *Bull. Am. Meteorol. Soc.* **2014**, *95*, 701–722. [[CrossRef](#)]
35. Seto, S.; Iguchi, T.; Oki, T. The basic performance of a precipitation retrieval algorithm for the global precipitation measurement mission’s single/dual-frequency radar measurements. *IEEE Trans. Geosci. Remote Sens.* **2013**, *51*, 5239–5251. [[CrossRef](#)]
36. Kazemzadeh, M.; Hashemi, H.; Jamali, S.; Uvo, C.B.; Berndtsson, R.; Huffman, G.J. Detecting the Greatest Changes in Global Satellite-Based Precipitation Observations. *Remote Sens.* **2022**, *14*, 5433. [[CrossRef](#)]
37. Hayden, L.; Liu, C. Differences in the diurnal variation of precipitation estimated by spaceborne radar, passive microwave radiometer, and IMERG. *J. Geophys. Res.* **2021**, *126*, e2020JD033020. [[CrossRef](#)]

38. Zhou, T.; Yu, R.; Chen, H.; Dai, A.; Pan, Y. Summer precipitation frequency, intensity, and diurnal cycle over China: A comparison of satellite data with rain gauge observations. *J. Clim.* **2008**, *21*, 3997–4010. [[CrossRef](#)]
39. Wang, J.; Xu, Y.; Yang, L.; Wang, Q.; Yuan, J.; Wang, Y. Data Assimilation of High-Resolution Satellite Rainfall Product Improves Rainfall Simulation Associated with Landfalling Tropical Cyclones in the Yangtze River Delta. *Remote Sens.* **2020**, *12*, 276. [[CrossRef](#)]
40. Chen, F.; Zeng, M.; Yu, L.; Zhuge, X.; Huang, H. Regional Variability in Microphysical Characteristics of Precipitation Features with Lightning across China: Observations from GPM. *Remote Sens.* **2022**, *14*, 6072. [[CrossRef](#)]
41. Chen, C.; Chen, Q.; Duan, Z.; Zhang, J.; Mo, K.; Li, Z.; Tang, G. Multiscale Comparative Evaluation of the GPM IMERG v5 and TRMM 3B42 v7 Precipitation Products from 2015 to 2017 over a Climate Transition Area of China. *Remote Sens.* **2018**, *10*, 944. [[CrossRef](#)]
42. Carbone, R.E.; Tuttle, J.D.; Ahijevych, D.A.; Trier, S.B. Inferences of predictability associated with warm season precipitation episodes. *J. Atmos. Sci.* **2002**, *59*, 2033–2056. [[CrossRef](#)]
43. Chen, G.; Sha, W.; Iwasaki, T.; Ueno, K. Diurnal variation of rainfall in the Yangtze River Valley during the spring-summer transition from TRMM measurements. *J. Geophys. Res.* **2012**, *117*, D06106. [[CrossRef](#)]
44. Liu, C.; Zipser, E.J.; Cecil, D.J.; Nesbitt, S.W.; Sherwood, S. A cloud and precipitation feature database from nine years of TRMM observations. *J. Appl. Meteor. Climatol.* **2008**, *47*, 2712–2728. [[CrossRef](#)]
45. Nesbitt, S.W.; Anders, A.M. Very high resolution precipitation climatologies from the Tropical Rainfall Measuring Mission precipitation radar. *Geophys. Res. Lett.* **2009**, *36*, L15815. [[CrossRef](#)]
46. Pope, M.; Jakob, C.; Reeder, M.J. Convective systems of the north Australian monsoon. *J. Clim.* **2008**, *21*, 5091–5112. [[CrossRef](#)]
47. Hirose, M.; Oki, R.; Shimizu, S.; Kachi, M.; Higashiuwatoko, T. Finescale diurnal rainfall statistics refined from eight years of TRMM PR data. *J. Appl. Meteor. Climatol.* **2008**, *47*, 544–561. [[CrossRef](#)]
48. Wang, C.; Chen, G.; Carbone, R. A climatology of warm-season cloud patterns over east Asia based on GMS infrared brightness temperature observations. *Mon. Wea. Rev.* **2004**, *132*, 1606–1629. [[CrossRef](#)]
49. Xu, W.; Zipser, E.J. Diurnal Variations of Precipitation, Deep Convection, and Lightning over and East of the Eastern Tibetan Plateau. *J. Clim.* **2011**, *24*, 448–465. [[CrossRef](#)]
50. Zhang, Y.; Zhang, F.; Davis, C.; Sun, J. Diurnal evolution and structure of long-lived mesoscale convective vortices along the Meiyu front over the east China plains. *J. Atmos. Sci.* **2018**, *75*, 1005–1025. [[CrossRef](#)]
51. Zhang, G.; Mao, J.; Liu, Y.; Wu, G. PV perspective of impacts on downstream extreme rainfall event of a Tibetan Plateau vortex collaborating with a Southwest China vortex. *Adv. Atmos. Sci.* **2021**, *38*, 1835–1851. [[CrossRef](#)]

Disclaimer/Publisher’s Note: The statements, opinions and data contained in all publications are solely those of the individual author(s) and contributor(s) and not of MDPI and/or the editor(s). MDPI and/or the editor(s) disclaim responsibility for any injury to people or property resulting from any ideas, methods, instructions or products referred to in the content.